Diffusional Features of a Lithium-Sulfur Battery Exploiting Highly-Microporous Activated Carbon

Fernando Luna Lama[a], Vittorio Marangon[b,c], Álvaro Caballero[a], Julián Morales[a]*, Jusef Hassoun[b,c,d]*

[a] Department of Química Inorgánica e Ingeniería Química, Instituto de Química Fina y Nanoquímica, University of Córdoba, 14071 Córdoba, Spain

[b] Department of Chemical, Pharmaceutical and Agricultural Sciences, University of Ferrara, Via Fossato di Mortara 17, Ferrara 44121, Italy

[c] Graphene Labs, Istituto Italiano di Tecnologia, Via Morego 30 – 16163 Genova, Italy.

[d] National Interuniversity Consortium of Materials Science and Technology (INSTM), University of Ferrara, Via Fossato di Mortara, 17, 44121, Ferrara, Italy.

*Corresponding authors: iq1mopaj@uco.es (Julián Morales), jusef.hassoun@unife.it, jusef.hassoun@iit.it (Jusef Hassoun).

Keywords

Supporting Information

Figure S1 reports the magnification of the low binding energy region of the XPS survey spectrum of the MPAC sample discussed in Figure 1 of the Manuscript. The figure shows the presence of peaks assigned to C, S and P, as well as a very weak signal assigned to Cl.
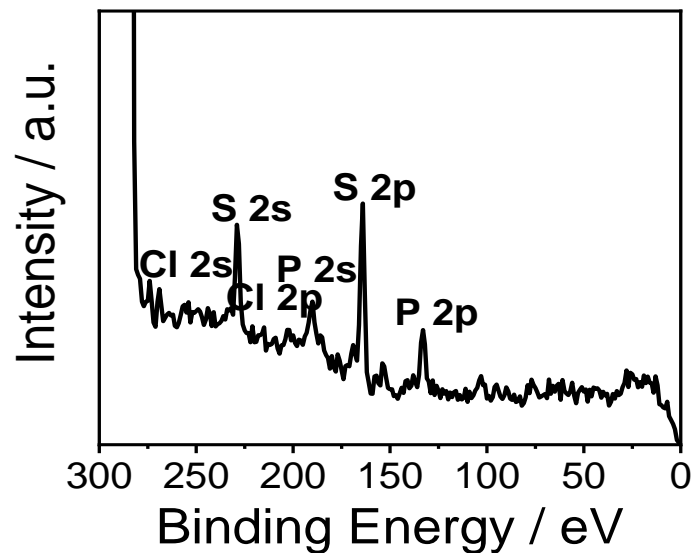

Figure S1. Magnification of the low binding energy region of the XPS survey spectra related to the MPAC sample. See Figure 1 in the Manuscript for more XPS data. See Experimental Section of the Manuscript for acronyms.

Figure S2 shows a morphological insight on the MPAC given by SEM images which exhibit agglomerated microparticles leading to interconnected pores, as typically observed in different activated carbons.
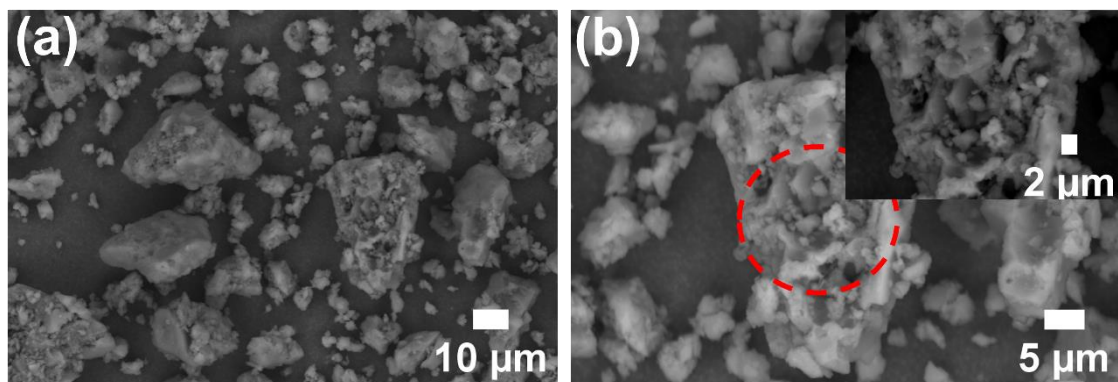

Figure S2. (a, b) SEM images at different magnifications of the MPAC sample, red circle in panel **(b)** and corresponding inset highlight the submicrometric morphology. See Experimental Section of the Manuscript for acronyms.

Figure S3 illustrates the EDS analysis performed on SEM image of the MPAC sample and reveals, beside the carbon, the presence of O, P, S and Cl elements with amounts slightly differing from those revealed by XPS (See Table 1 and discussion in the Manuscript), while N is not detected.
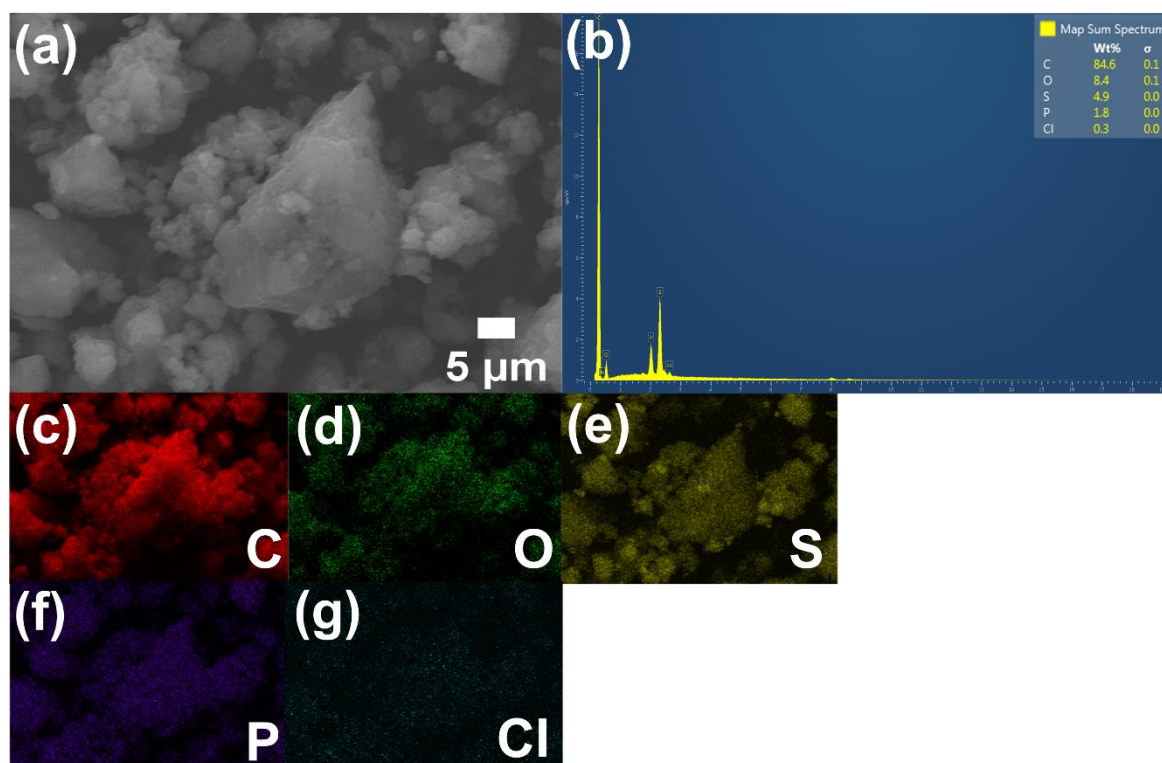

Figure S3. SEM-EDS study of the MPAC sample. In detail: **(a)** SEM image acquired through secondary electron mode; **(b)** EDS spectrum; **(c-g)** EDS elemental maps related to **(c)** C, **(d)** O, **(e)** S, **(f)** P and **(g)** Cl. See Experimental Section of the Manuscript for acronyms.

Figure S4 represents the synthesis of the activated carbon (MPAC) and the related sulfur composites. The carbonization of the mango pits precursor and the subsequent activation through H_3PO_4 lead to a carbon material benefitting from disordered structure and a complex system of micropores that well accommodate sulfur. Indeed, simple mixing at 120 °C between carbon and sulfur (see Experimental Section in the Manuscript) allows synthesis of three composites where the active material is tuned to either 70% (S@MPAC-73), 80% (S@MPAC-82) or 90% (S@MPAC-91) in weight ratio with respect to the MPAC.
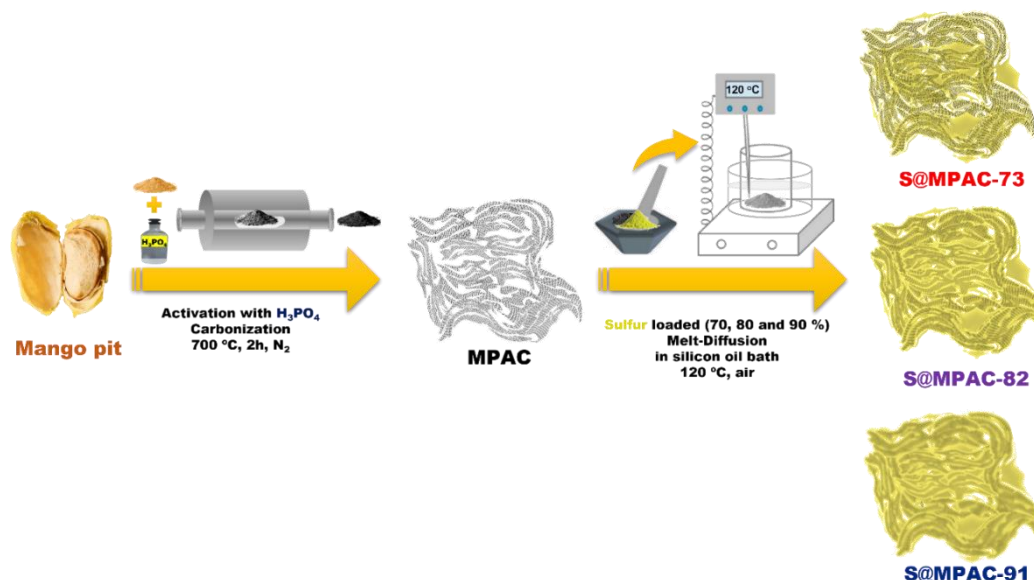
Figure S4. Graphical representation of the S@MPAC-73, S@MPAC-82, and S@MPAC-91 composites synthesis. See experimental section for acronyms and synthesis details.

Figure S5 illustrates the differential curves (DTG) of the TGA profiles reported in Figure 3b of the manuscript. The DTG of pure S shows one only peak, while the composites reveal a peak and an additional high-temperature shoulder having an intensity decreasing by the S content increase.
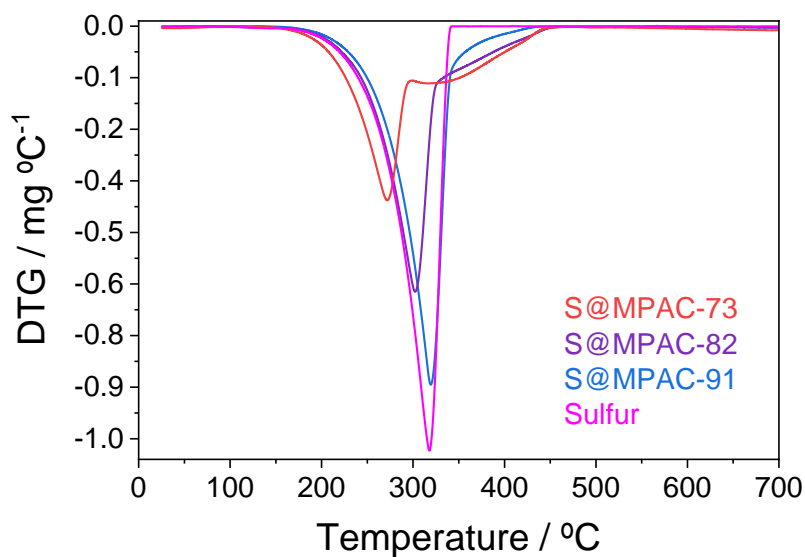
Figure S5. Differential thermogravimetry (DTG) related to the TGA reported in Figure 3b in the Manuscript of S@MPAC-73 (red), S@MPAC-82 (violet), S@MPAC-91 (blue), and elemental sulfur (magenta) performed under N_2 atmosphere from 25 to 700 °C. See Experimental Section of the Manuscript for acronyms.

Figure S6 reports the EDS mapping performed on SEM images of S@MPAC-73 (Figure S6a, d), S@MPAC-82 (Figure S6b, e), and S@MPAC-91 (Figure S6c, f). The figure evidences a very homogeneous distribution of the sulfur into the carbon matrix, with a magnitude increasing by increasing the sulfur content in the S@MPAC composite from 70 wt. % (Figure S6d) to 80 wt. % (Figure S6e) and to 90 wt. % (Figure S6f).
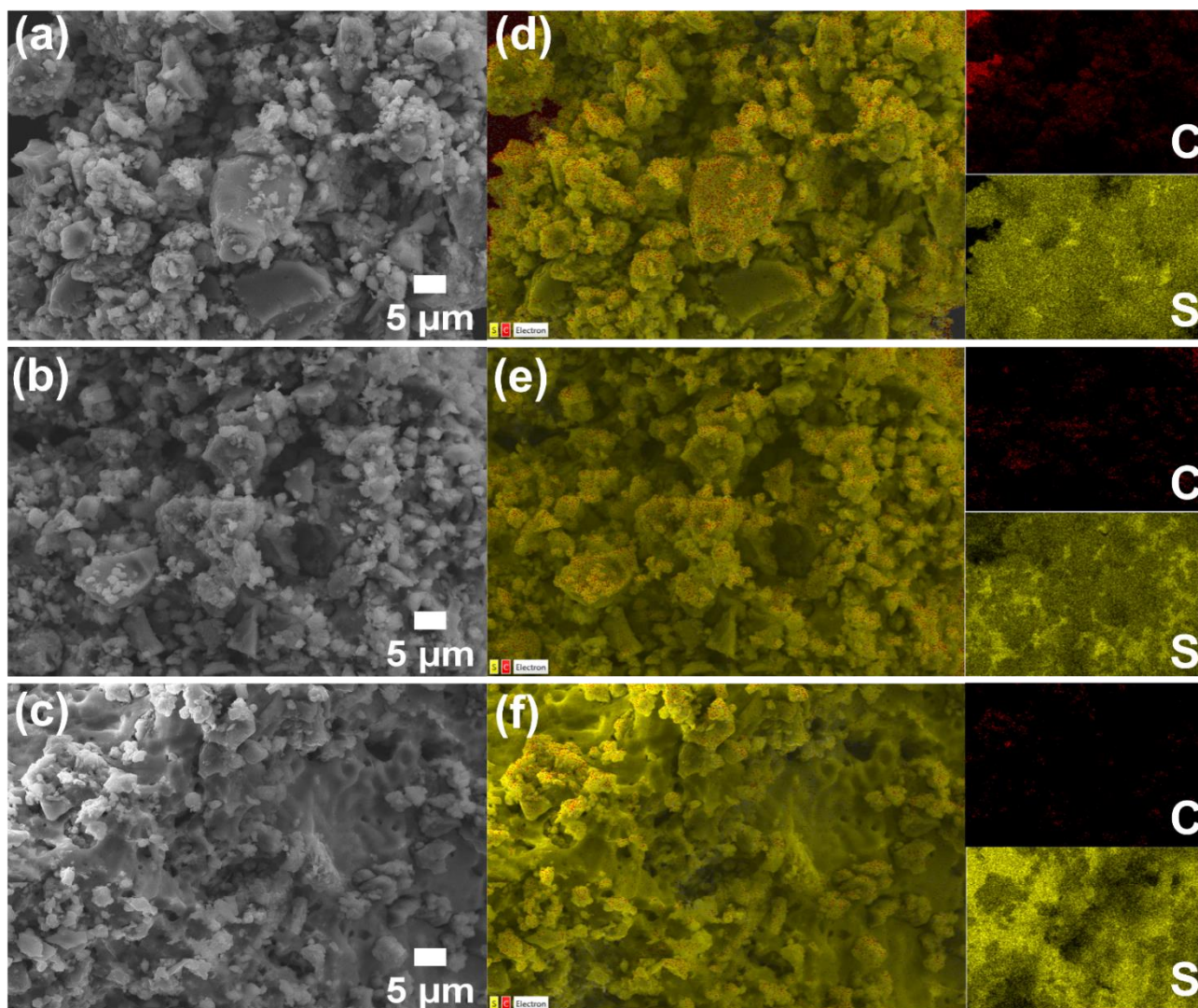
Figure S6. (a-c) SEM images and **(d-f)** EDS elemental maps showing C and S distribution related to the **(a, d)** S@MPAC-73, **(b, e)** S@MPAC-82 and **(c, f)** S@MPAC-91 composites. Right-hand corresponding insets display the single C and S EDS elemental maps. See Experimental Section of the Manuscript for acronyms.

Figure S7 displays the linear fits for lithium cells using S@MPAC-73 (Figure S7a), S@MPAC-82 (Figure S7b), and S@MPAC-91 (Figure S7c) of the curves reporting the peak current intensity (I_{peak}) and the related square root of the scan rate ($v^{1/2}$) values obtained from the corresponding CV profiles in the Manuscript (Figure 6a-c), used to determine D_{CV} according to Randles-Sevcik equation[1] (equation 1 in the Manuscript) in the reduction peaks labelled with 1 and 2, and the oxidation ones labelled with 3 and 4. See the discussion of Figure 6 in the Manuscript for further details.
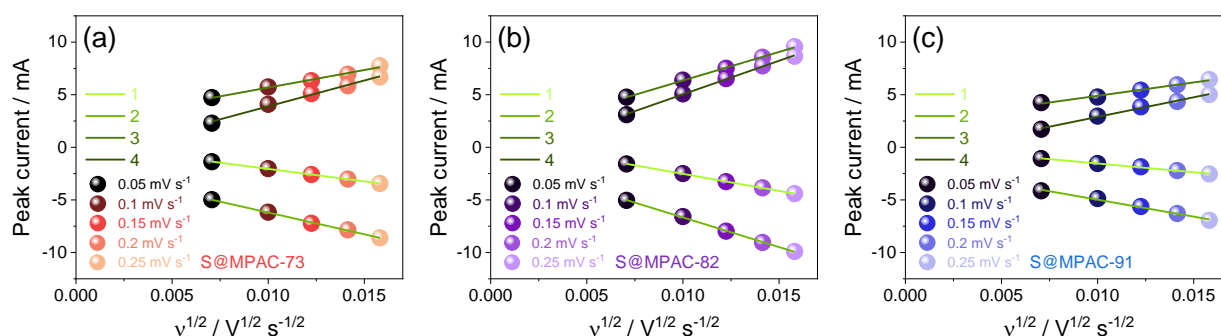
Figure S7. Linear fits of peak current intensity (I_{peak}) *vs.* the square root of the scan rate ($v^{1/2}$) for Li|DOL:DME, 1 mol kg^{-1} LiTFSI, 1 mol kg^{-1} LiNO$_3$|cathode cells using (**a**) S@MPAC-73, (**b**) S@MPAC-82, and (**c**) S@MPAC-91 obtained from corresponding CV (see Figure 6a-c, and Tab. 3 in the Manuscript for the potential values of the selected CV peaks labeled with numbers herein). The slope of the linear fits is used in Randles-Sevcik equation[1] (Equation 1 in the Manuscript) to calculate the Li$^+$ diffusion coefficients (D_{CV}, see also Figure 6a in the Manuscript). See Experimental Section of the Manuscript for acronyms.

Figure S8 illustrates linear plots related to cells using S@MPAC-73 (Figure S8a-d), S@MPAC-82 (Figure S8e-h), and S@MPAC-91 (Figure S8i-l) of the real and the imaginary components of the of complex impedance $Z_W^* = \sigma\omega^{-1/2} - j\sigma\omega^{-1/2}$ (i.e., Z_{re} and Z_{im}, respectively) as function of $\omega^{-1/2}$ within the semi-infinite diffusion condition (Warburg region) represented by the line tilted at 45° in the low-frequency region in the corresponding Nyquist graphs in Figure 6d-f in the Manuscript recorded by EIS in the CV peaks 1, 2, 3 and 4, respectively. These plots allow the achievement the pre-exponential factor σ used to determine D_{EIS} according to equation 2 in the Manuscript.[2]
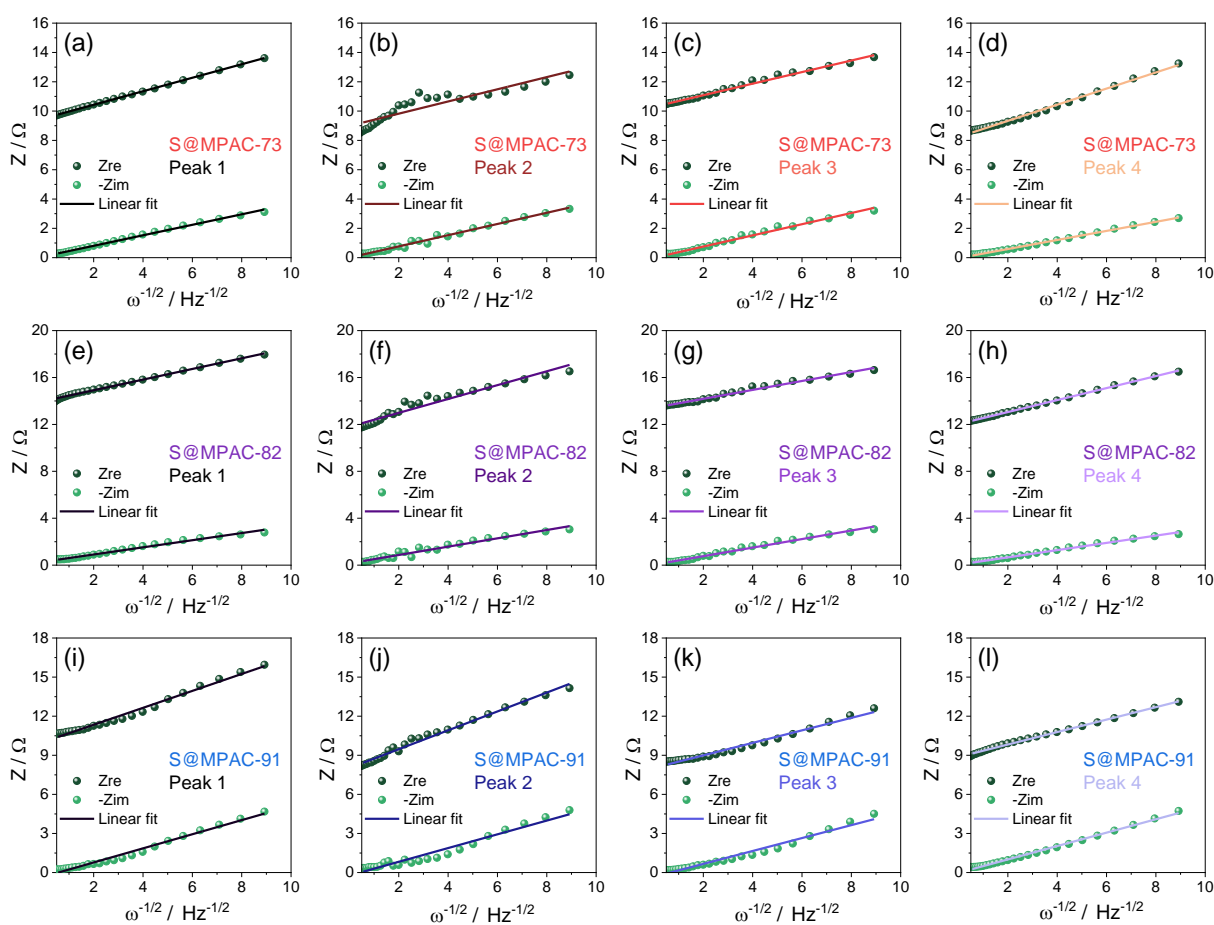
**Figure S8.** Linear fits related to Li|DOL:DME, 1 mol kg^{-1} LiTFSI, 1 mol kg^{-1} LiNO$_3$|cathode cells using **(a-d)** S@MPAC-73, **(e-f)** S@MPAC-82, and **(i-l)** S@MPAC-91 at various CV states of charge of the real and imaginary impedance components *vs.* $\omega^{-1/2}$ in the Warburg region of the Nyquist plots in Figure 6 **(d-f)** used for the calculation of the Li$^+$ diffusion coefficients through equation (2) (D_{EIS}, see also Figure 7b in the Manuscript).[2] See Tab. 3 for the selected potential values to perform EIS upon CV. See Experimental Section of the Manuscript for acronyms.

Figure S9 reports in comparison the potential vs. time curves (panel a), a current pulse with diffusion time $t \ll \tau$ related to $x = 0.1$ (panel b), and corresponding E vs $t^{1/2}$ linear fitting (panel c) used to calculate $\mathrm{d}E/\mathrm{d}t^{1/2}$ for the determination of D_{GITT} from equation (3)[3] in the Manuscript and the plots in Figure 6g-i.
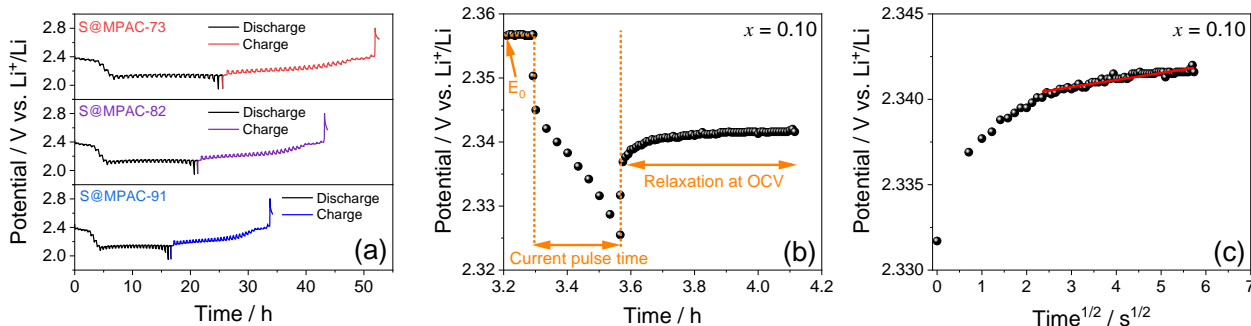
Figure S9. (a) GITT curves reported in the potential *vs.* time scale related to Li|DOL:DME, 1 mol kg^{-1} LiTFSI, 1 mol kg^{-1} LiNO$_3$|cathode cells employing S@MPAC-73 (top), S@MPAC-82 (intermediate), and S@MPAC-91 (bottom) electrodes; **(b)** detailed view on a single GITT pulse reported in the potential *vs.* time for $x = 0.1$ (where x is the exchanged lithium ions within Li$_{2x}$S), **(c)** the same step in potential *vs.* square root of time scale used to calculate $\mathrm{d}E/\mathrm{d}t^{1/2}$ for the determination of D_{GITT} from equation (3) in the manuscript and the plots in Figure 6g-i.[3]

Figure S10 shows the voltage profile (a) and corresponding cycling trend (b) of a lithium cell using the S@MPAC-91 electrode with a sulfur loading increased to 11 mg cm^{-2} and E/S ratio of 5 µL mg^{-1} tested at C/20 in order to achieve Li-S cell operation into practical condition.
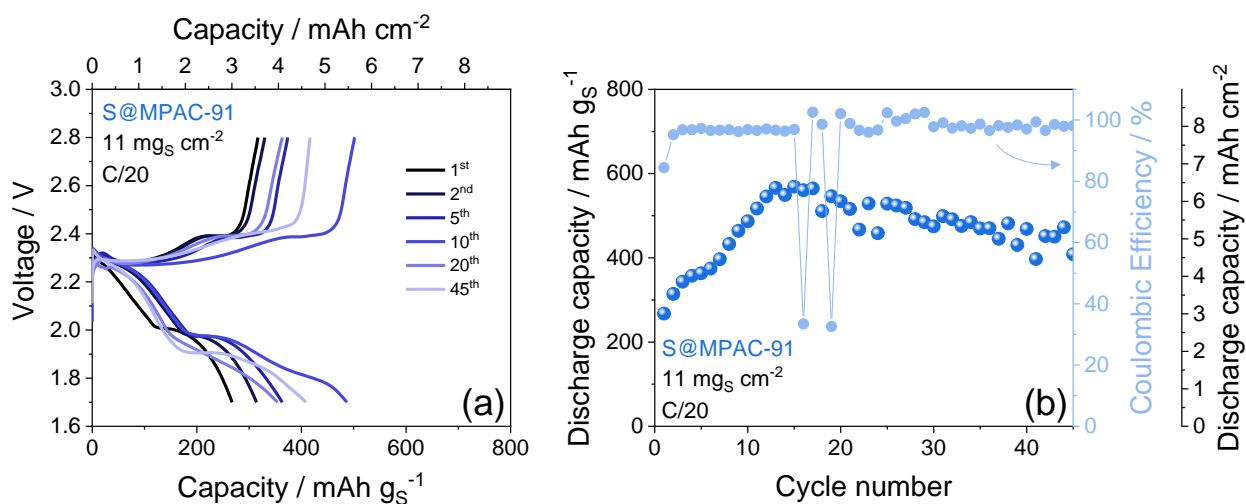
Figure S10. (a) Voltage profiles (top *x*-axis displays areal capacity) and **(b)** corresponding cycling trend (right-hand *y*-axes show coulombic efficiency and areal discharge capacity) related to a Li|DOL:DME, 1 mol kg^{-1} LiTFSI, 1 mol kg^{-1} LiNO$_3$|S@MPAC-91 cell cycled a the constant C-rate of C/20 (1C = 1675 mA g^{-1}). Voltage range: 1.7 – 2.8 V. Cathode sulfur loading: 11 mg cm^{-2} (area: 1.54 cm^{-2}). E/S ratio: 5 µL mg^{-1}.

References

[1]   A. Benítez, V. Marangon, C. Hernández-Rentero, Á. Caballero, J. Morales, J. Hassoun, *Mater Chem Phys* **2020**, *255*, 123484.

[2]   D. Di Lecce, T. Hu, J. Hassoun, *J Alloys Compd* **2017**, *693*, 730.

[3]   D. Di Lecce, J. Hassoun, *Journal of Physical Chemistry C* **2015**, *119*, 20855.